

# Electronic Supplementary Information

## Precursor chemistry matters in boosting photoredox activity of graphene/semiconductor composites

Min-Quan Yang, Chuang Han, Nan Zhang, and Yi-Jun Xu\*

State Key Laboratory of Photocatalysis on Energy and Environment, College of Chemistry, Fuzhou University, Fuzhou, 350002, P. R. China & College of Chemistry, New Campus, Fuzhou University, Fuzhou, 350108, P. R. China.

\* To whom correspondence should be addressed.

E-mail: [yjxu@fzu.edu.cn](mailto:yjxu@fzu.edu.cn)

### Contents list

#### Experimental details

**Fig. S1.** The corresponding height profiles along the yellow lines drawn in **Fig. 1A, B and D**.

**Fig. S2.** The zeta potentials of GO and GO-A dispersed in deionized water with the concentration of *ca.* 0.2 mg mL<sup>-1</sup>.

**Fig. S3.** The colloidal dispersions of GO and GO-A with the concentration of *ca.* 0.75 mg mL<sup>-1</sup> centrifuged at 3000, 6000, 9000 and 12000 rpm for 8 min, respectively.

**Fig. S4.** The dispersions of GR and GR-A with ultrasonication for 15 min in water and then standing for 1 h at ambient conditions.

**Fig. S5.** The electrochemical impedance spectroscopy (EIS) Nyquist plots of GR and GR-A in the dark.

**Fig. S6.** X-ray diffraction patterns of CdS/GR (A) and CdS/GR-A (B) nanocomposites with different weight addition ratios of graphene.

**Table S1.** The average crystallite sizes of CdS nanoparticles in blank CdS, GR/CdS and CdS/GR-A nanocomposites calculated from the (111), (220) and (311) facet diffraction peaks of cubic CdS on the basis of Scherrer's formula.

**Fig. S7.** UV-vis diffuse reflectance (DRS) spectra of CdS/GR (A) and CdS/GR-A (B) nanocomposites with different weight addition ratios of graphene.

**Fig. S8.** SEM images of CdS/5% GR (A, B) and CdS/5%GR-A (C, D).

**Fig. S9.** Raman spectra of CdS/5%GR and CdS/5%GR-A (A), and Raman spectra of D and G bands of CdS/5%GR and CdS/5%GR-A nanocomposites (B).

**Fig. S10.** Control experiments of photocatalytic selective reduction of 4-nitroaniline (4-NA) over the optimal samples of CdS/5%GR and CdS/5%GR-A with different reaction conditions under visible light irradiation ( $\lambda > 420$  nm); AO (ammonium oxalate) is the scavenger for photogenerated holes and  $K_2S_2O_8$  is the scavenger for photogenerated electrons.

**Fig. S11.** Control experiments of photocatalytic selective oxidation of benzyl alcohol with the addition of different radical scavengers: ammonium oxalate (AO, scavenger for holes), benzoquinone (BQ, scavenger for superoxide radicals),  $K_2S_2O_8$  (scavenger for electrons) and tert-butyl alcohol (TBA, scavenger for hydroxyl radicals) over the optimum samples of CdS/5%GR and CdS/5%GR-A under visible light irradiation ( $\lambda > 420$  nm) for 1 h.

**Fig. S12.** Time-online profiles of conversion of benzylic alcohols over the as-synthesized CdS/5%GR and CdS/5%GR-A nanocomposites under visible light irradiation ( $\lambda > 420$  nm): 4-nitrobenzyl alcohol (A); 4-fluorobenzyl alcohol (B); 4-chlorobenzyl alcohol (C); 4-methylbenzyl alcohol (D) and 4-methoxybenzyl alcohol (E).

**Fig. S13.** Photocatalytic reduction of different nitroaromatic compounds over the as-synthesized CdS/5%GR and CdS/5%GR-A under visible light irradiation ( $\lambda > 420$  nm) with the addition of ammonium oxalate as a quencher for photogenerated holes in  $N_2$  atmosphere at room temperature: 2-nitroaniline (A); 4-nitrophenol (B); 1-chloro-4-nitrobenzene (C); 1-bromo-4-nitrobenzene (D); 4-nitrotoluene (E) and 4-nitroanisole (F).

**Fig. S14.** Comparison of photocatalytic selective oxidation of benzyl alcohol to benzaldehyde (A) and reduction of 4-nitroaniline (4-NA) to p-phenylenediamine (B) over blank CdS, CdS/5% GR, CdS/5% GR-A and optimal CdS/(GR-M) ( $M = Ca^{2+}, Cr^{3+}, Mn^{2+}, Fe^{2+}, Co^{2+}, Ni^{2+}, Cu^{2+},$  and  $Zn^{2+}$ ) nanocomposites under visible light irradiation ( $\lambda > 420$  nm) for 60 min.

**Scheme S1.** Schematic description for photocatalytic redox processes over the CdS/graphene nanocomposites.

**Fig. S15.**  $N_2$  adsorption-desorption isotherms of CdS/5%GR and CdS/5%GR-A.

**Fig. S16.** Bar plot showing the remaining benzyl alcohol (BA) and 4-nitroaniline (4-NA) in reaction solution after being kept in dark for 2 h to achieve the adsorption-desorption equilibrium over CdS/5%GR and CdS/5%GR-A.

**Fig. S17.** Photograph of the experimental setup for photocatalytic aerobic oxidation of alcohols.

**Fig. S18.** Photograph of the experimental setup for photocatalytic anaerobic reduction of nitroaromatic compounds.

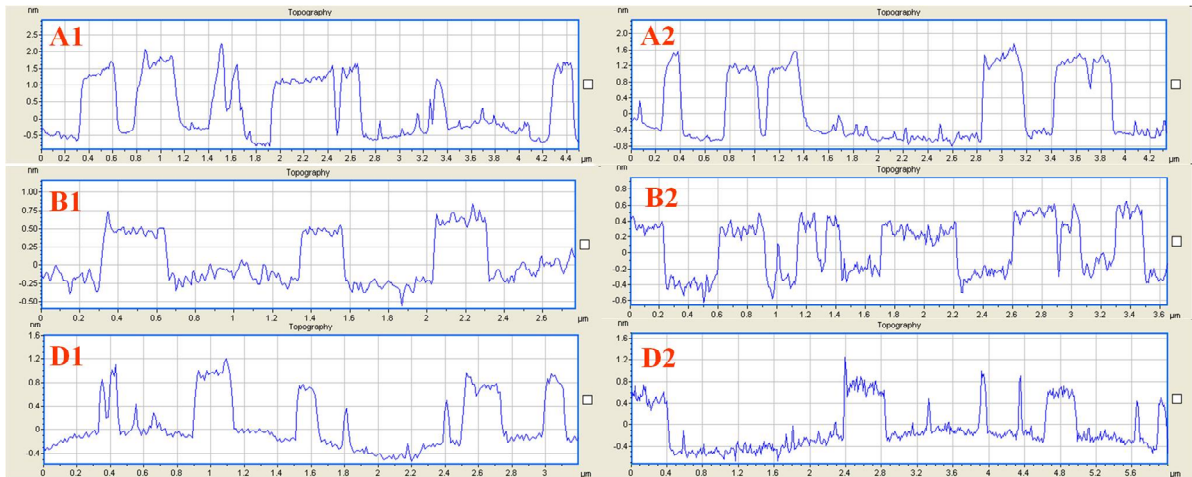


**Fig. S1.** The corresponding height profiles along the yellow lines drawn in **Fig. 1A, B** and **D**.

**Note:** As can be seen from **Fig. S1**, the corresponding height profiles along the yellow lines drawn in **Fig. 1A, B** and **D** show that the original GO displays an average thickness of about 1.8 nm (**A1, A2**) or 0.9 nm (**B1, B2**), which are comparable to the previously reported thickness of bi- or monolayer graphene oxide nanosheets, respectively. As for the sample of GO-A, the height profiles (**C1, C2**) show that the average thickness of the relatively large graphene oxide nanosheets is about 0.9 nm, corresponding to the thickness of monolayer graphene oxide. The result indicates that the graphene oxide nanosheets in GO-A are less likely to aggregate after the acid treatment as compared to that in the original GO.

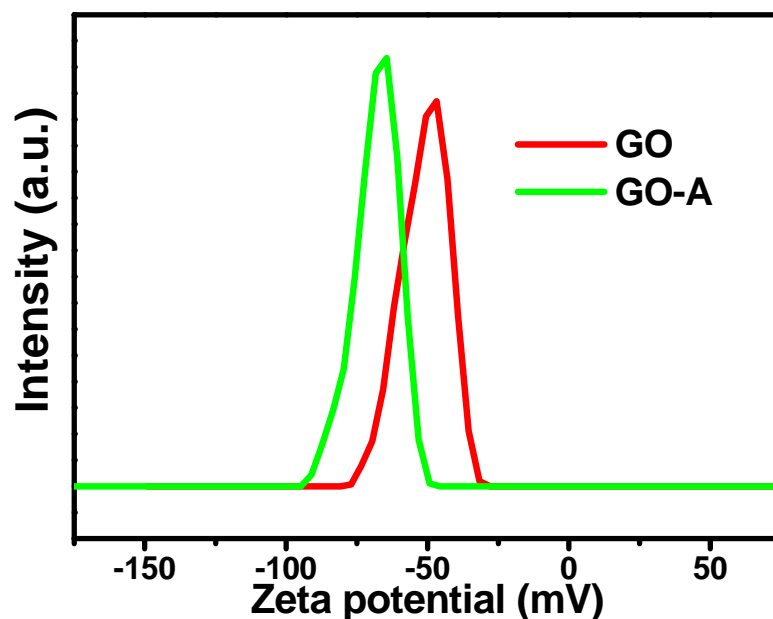


**Fig. S2.** The zeta potentials of GO and GO-A dispersed in deionized water with the concentration of *ca.* 0.2 mg mL<sup>-1</sup>.

**Note:** Fig. S2 shows the zeta potential ( $\xi$ ) analysis result of GO and GO-A samples dispersed in deionized water. It can be seen that the dispersion of original GO in water reveals a strong negatively charged surface with a zeta potential value of -51.2 mV. After the ultrasonic treatment of GO with acid, the obtained GO-A shows a more negative zeta-potential value of -67.4 mV. This is mainly due to that the ultrasonication of GO with acid further increases the oxidation degree and introduces more oxygenated functional groups (*e.g.* epoxy, carboxyl and hydroxyl groups) on the surface of GO-A in comparison with that of original GO, thereby endowing the GO-A nanosheets with higher charge density, and thus displaying more negative zeta-potential value.



**Fig. S3.** The colloidal dispersions of GO and GO-A with the concentration of *ca.*  $0.75 \text{ mg mL}^{-1}$  centrifuged at 3000, 6000, 9000 and 12000 rpm for 8 min, respectively.

**Note:** The colloidal stability of the original GO and GO-A dispersions has been evaluated by the centrifugation test. As shown in **Fig. S3**, the dispersions of original GO and GO-A with the concentration of *ca.*  $0.75 \text{ mg mL}^{-1}$  are both subject to centrifugation at 3000, 6000, 9000, to 12000 rpm for 8 min, respectively. It can be seen that the original GO start to sediment from 6000 rpm while the GO-A dispersion is relatively stable after being centrifuged at 9000 rpm, indicating that the GO-A aqueous dispersion displays much enhanced colloidal stability than original GO.

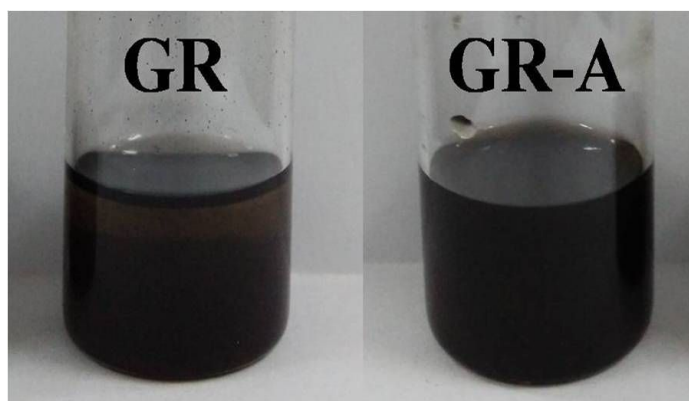


**Fig. S4.** The dispersions of GR and GR-A with ultrasonication for 15 min in water and then standing for 1 h at ambient conditions.

**Note:** Fig. S4 shows the result of the dispersibility test of GR and GR-A obtained from the solvothermal reduction of GO and GO-A, respectively. It has been found that after being sonicated for 15 min in deionized water and then standing for 1 h at ambient conditions, the original GO deposits obviously. In contrast, the GR-A sample disperse quite well in deionized water and no obvious precipitation has been observed. The higher dispersibility of GR-A than that of GR can be ascribed to the fact that the GR-A sheets with smaller lateral sizes are less likely to aggregate due to the reduced overlapping area and decreased  $\pi$ - $\pi$  stacking interaction energies between graphene nanosheets.

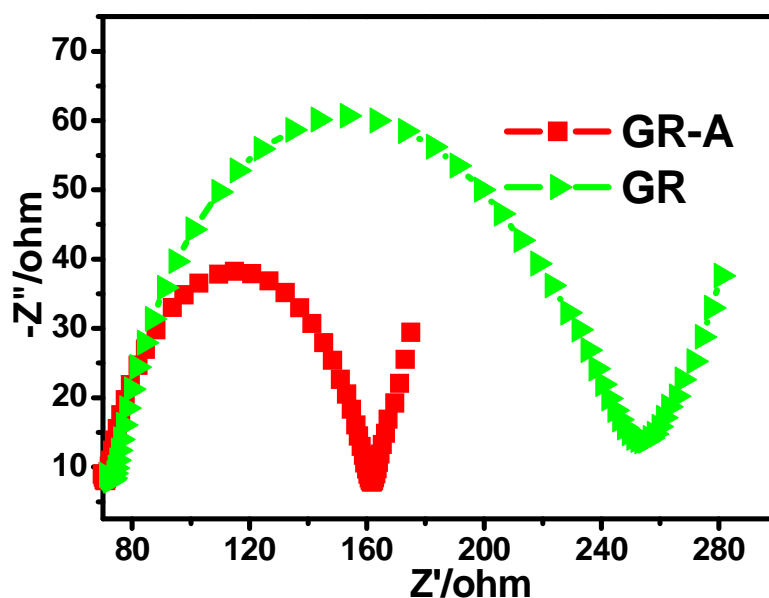


**Fig. S5.** The electrochemical impedance spectroscopy (EIS) Nyquist plots of GR and GR-A in the dark.

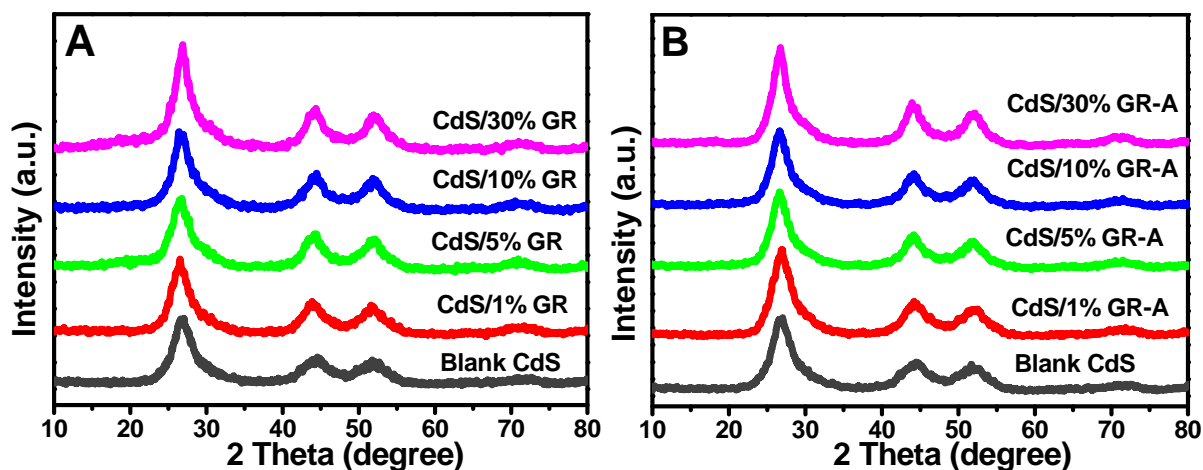


**Fig. S6.** X-ray diffraction patterns (XRD) of CdS/GR (A) and CdS/GR-A (B) nanocomposites with different weight addition ratios of graphene.

**Table S1.** The average crystallite sizes of CdS nanoparticles in blank CdS, GR/CdS and CdS/GR-A nanocomposites calculated from the (111), (220) and (311) facet diffraction peaks of cubic CdS on the basis of Scherrer's formula.

CdS/GR		CdS/GR-A	
GR content (wt. %)	Average crystallite sizes (nm)	GR-A content (wt. %)	Average crystallite sizes (nm)
0 %	2.0	0 %	2.0
1 %	2.4	1 %	2.3
5 %	2.7	5 %	2.5
10 %	2.7	10 %	2.7
30 %	2.9	30 %	2.8

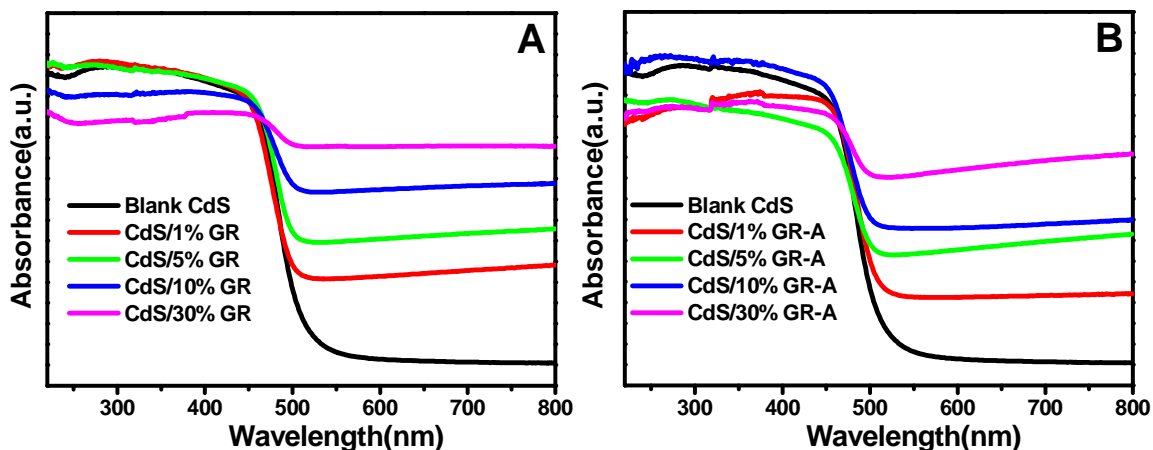


**Fig. S7.** UV-vis diffuse reflectance (DRS) spectra of CdS/GR (A) and CdS/GR-A (B) nanocomposites with different weight addition ratios of graphene.

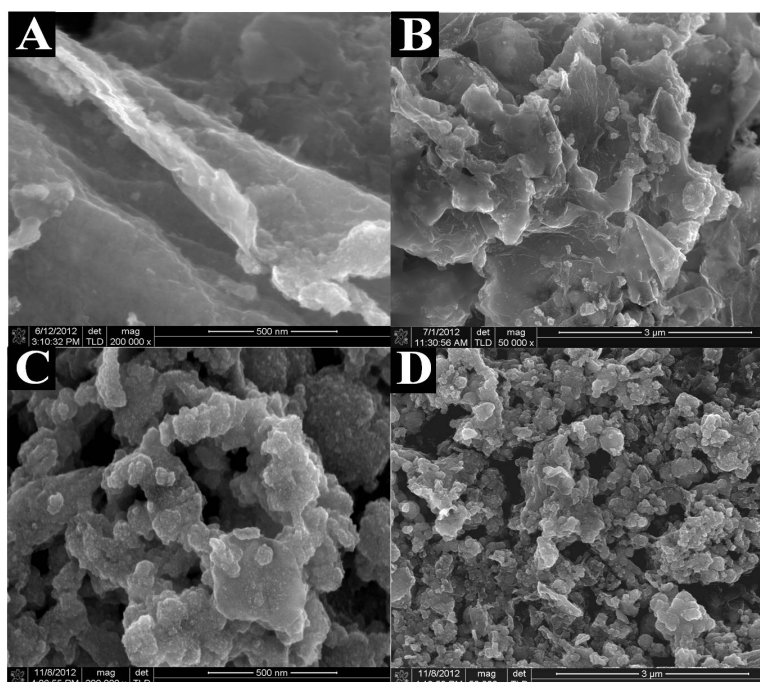


**Fig. S8.** SEM images of CdS/5%GR (A, B) and CdS/5%GR-A (C, D).

**Note:** Fig. S8 A-B displays the typical SEM images of CdS/5%GR, from which the large sheet structure can be clearly distinguished. However, for the sample of CdS/5%GR-A, as shown in Fig. S8 C-D, no apparently large sheet structure can be observed. This is reasonable because the morphology and size of the graphene oxide nanosheets has been drastically changed in GO and GO-A (the precursors of GR and GR-A). The GO-A with significantly decreased lateral sizes makes it hard to obtain large sheet structure in the synthesized CdS/GR-A nanocomposites. The morphology difference between the CdS/5%GR and CdS/5%GR-A is well in accordance with the TEM analysis result.

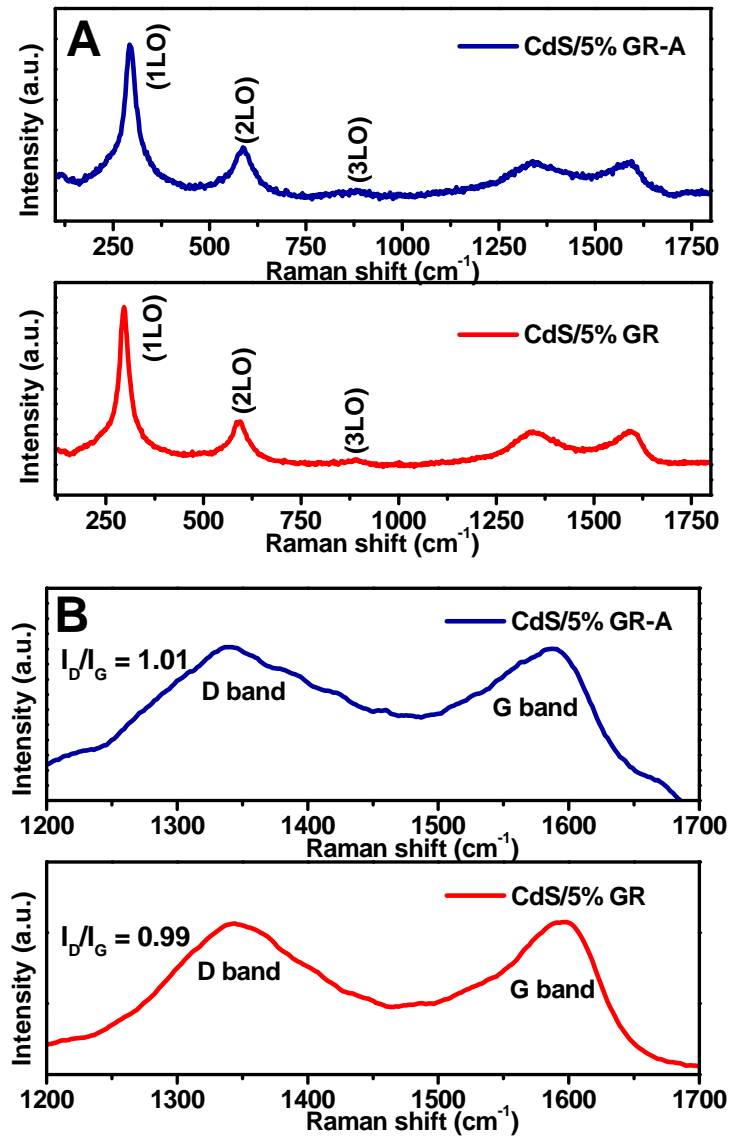


**Fig. S9.** Raman spectra of CdS/5% GR and CdS/5% GR-A (A), and Raman spectra of D and G band of CdS/5% GR and CdS/5% GR-A nanocomposites (B).

**Note:** The characteristic Raman mode of cubic CdS can be readily identified in **Fig. S9A**, whereas the characteristic D band and G bands of graphene are distinct in **Fig. S9B**.

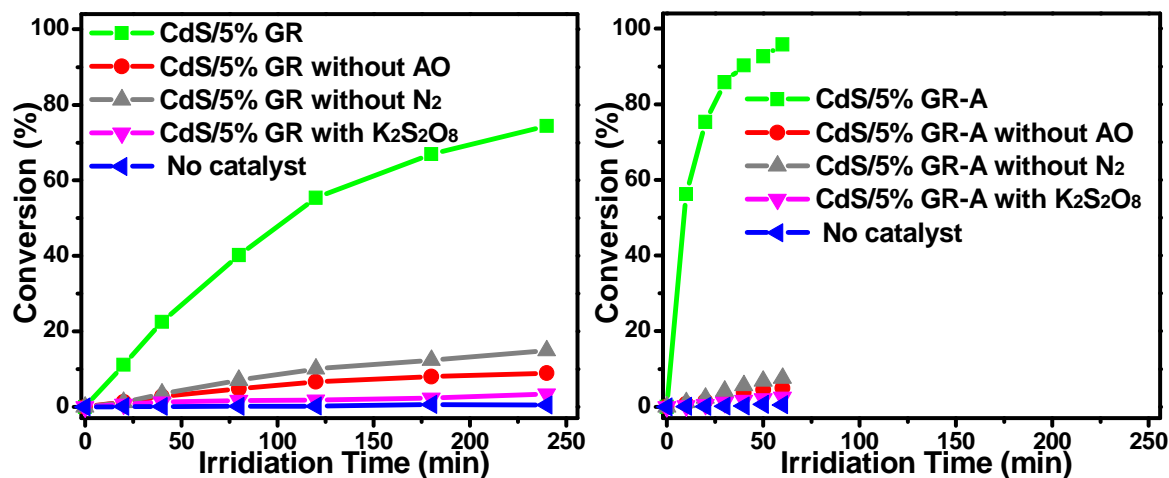


**Fig. S10.** Control experiments of photocatalytic selective reduction of 4-nitroaniline (4-NA) over the optimal samples of CdS/5% GR and CdS/5% GR-A with different reaction conditions under visible light irradiation ( $\lambda > 420$  nm); AO (ammonium oxalate) is the scavenger for photogenerated holes and  $K_2S_2O_8$  is the scavenger for photogenerated electrons.

**Note:** Fig. S10 shows the photocatalytic activities of CdS/5%GR and CdS/5%GR-A for selective reduction of 4-nitroaniline (4-NA) under different controlled reaction conditions. Initial blank experiment in the absence of photocatalyst shows no conversion of 4-NA, which ensures that the reaction is really driven by a photocatalytic process. When a radical scavenger  $K_2S_2O_8$  for photogenerated electrons is added into the reaction system,<sup>S1,S4</sup> no obvious conversion of 4-NA can be observed, clearly demonstrating that the photogenerated electrons play a decisive role in driving the photocatalytic reduction of nitroaromatic compounds. In addition, when the photocatalytic reaction is performed in the absence of  $N_2$  or hole scavenger of AO,<sup>S1</sup> the conversions of 4-NA over the CdS/5%GR and CdS/5%GR-A are also strongly inhibited, indicating that the inert atmosphere and hole scavenger are both indispensable for the photocatalytic reduction of nitroaromatic compounds over the CdS/graphene nanocomposites.

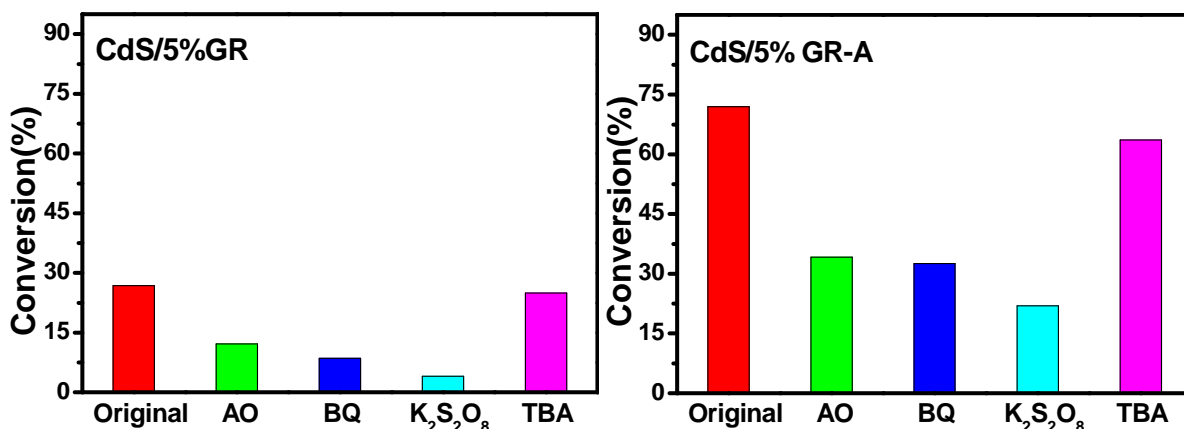


**Fig. S11.** Control experiments of photocatalytic selective oxidation of benzyl alcohol with the addition of different radical scavengers: ammonium oxalate (AO, scavenger for holes), benzoquinone (BQ, scavenger for superoxide radicals), K<sub>2</sub>S<sub>2</sub>O<sub>8</sub> (scavenger for electrons) and tert-butyl alcohol (TBA, scavenger for hydroxyl radicals) over the optimum samples of CdS/5%GR and CdS/5%GR-A under visible light irradiation ( $\lambda > 420$  nm) for 1 h.

**Note:** Fig. S11 shows the photocatalytic activities of CdS/5%GR and CdS/5%GR-A for selective oxidation of benzyl alcohol in the presence of different radical scavengers. From the data, we can see that when AO scavenger for holes ( $h^+$ ) is added,<sup>S1, S2</sup> the conversion of benzyl alcohol is significantly prohibited. When BQ scavenger for superoxide radicals ( $O_2^{\bullet-}$ ) or K<sub>2</sub>S<sub>2</sub>O<sub>8</sub> scavenger for electrons ( $e^-$ ) is added,<sup>S1</sup> the conversion of benzyl alcohol is also decreased remarkably. This can be ascribed to that although photogenerated electrons can not directly participate in the oxidation process, they can activate molecular oxygen, *e.g.*, to generate superoxide radicals ( $O_2^{\bullet-}$ ). Consequently, this leads to the observation that the conversion of benzyl alcohol is markedly inhibited when adding BQ scavenger for superoxide radicals ( $O_2^{\bullet-}$ ) or K<sub>2</sub>S<sub>2</sub>O<sub>8</sub> scavenger for electrons into the photocatalytic reaction system. Additionally, when the TBA scavenger for hydroxyl radicals ( $\cdot OH$ ) is added into the reaction system, the conversion of benzyl alcohol is decreased slightly, which is in faithful accordance with the previous work that hydroxyl radicals is absent in the benzotrifluoride (BTF) solvent.<sup>S1, S3</sup> The analogous phenomena are observed for both CdS/5%GR and CdS/5%GR-A. Therefore, the results from control experiments clearly suggest that for oxidation of benzylic alcohols over CdS/5%GR and CdS/5%GR-A, the primary active radical species are photogenerated holes, electrons, and activated oxygen (*e.g.*, superoxide radicals).

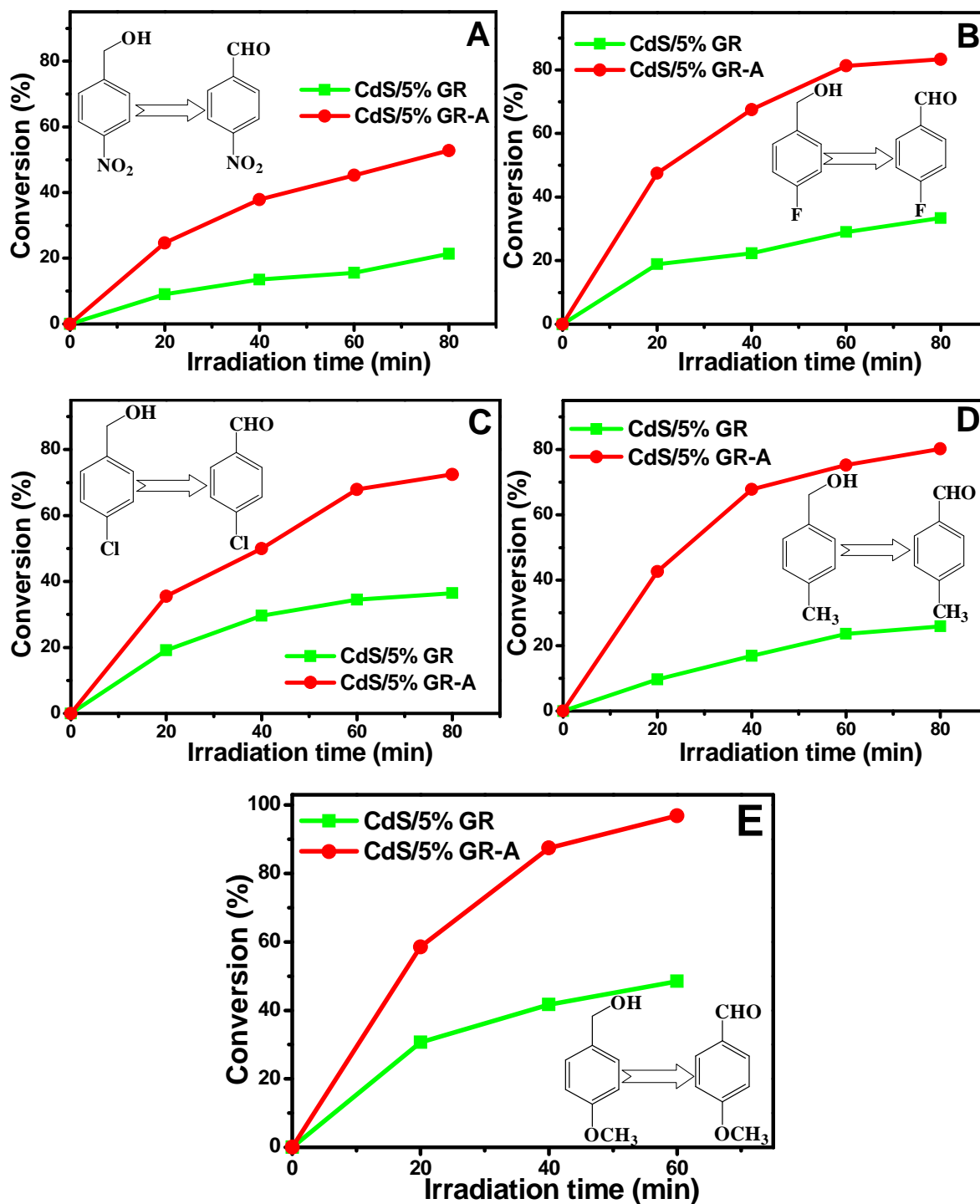


**Fig. S12.** Time-online profiles of conversion of benzylic alcohols over the as-synthesized CdS/5%GR and CdS/5%GR-A nanocomposites under visible light irradiation ( $\lambda > 420$  nm): 4-nitrobenzyl alcohol (A); 4-fluorobenzyl alcohol (B); 4-chlorobenzyl alcohol (C); 4-methylbenzyl alcohol (D) and 4-methoxybenzyl alcohol (E).

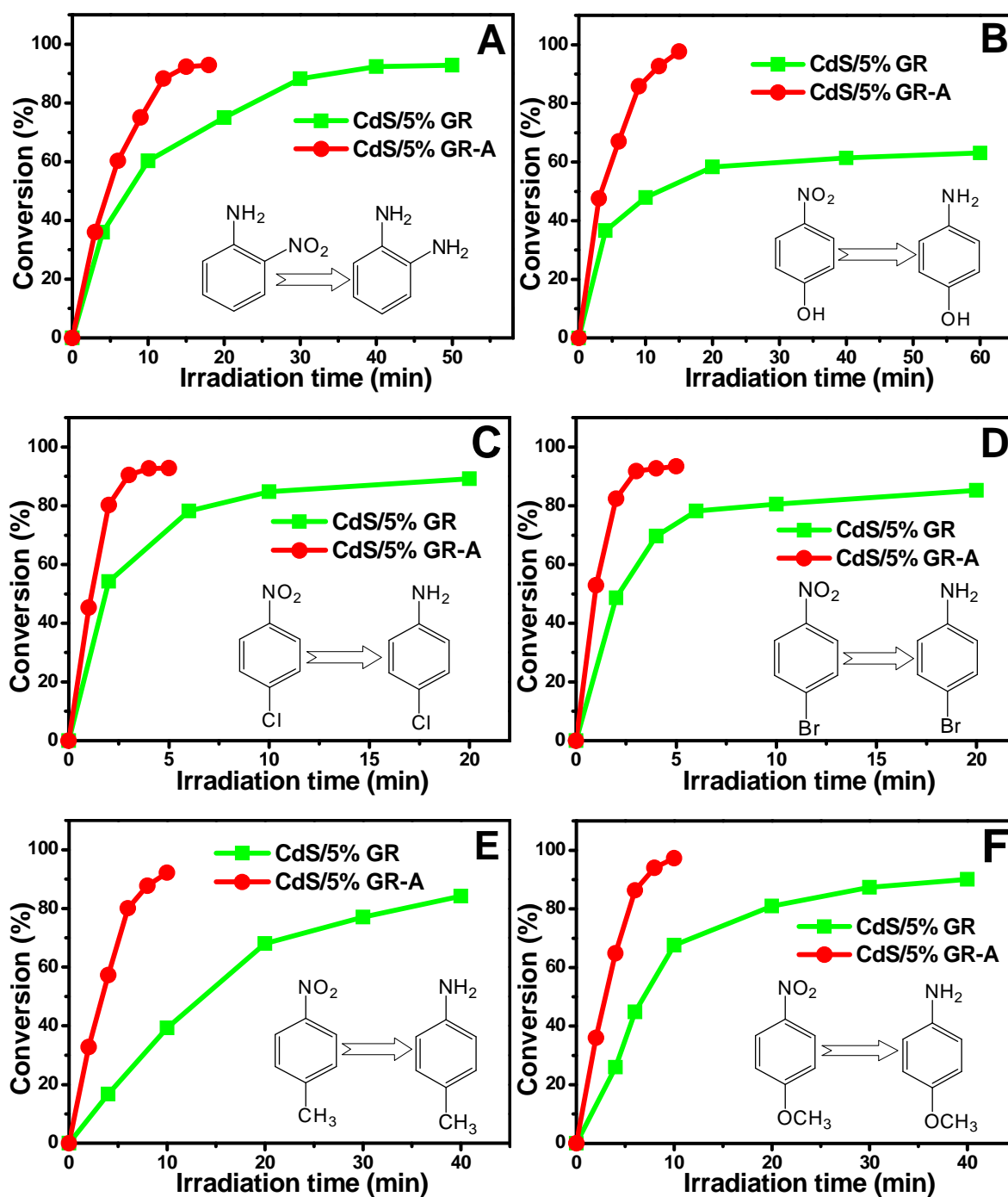


**Fig. S13.** Photocatalytic reduction of different nitroaromatic compounds over the as-synthesized CdS/5%GR and CdS/5%GR-A under visible light irradiation ( $\lambda > 420$  nm) with the addition of ammonium oxalate as a quencher for photogenerated holes in  $N_2$  atmosphere at room temperature: 2-nitroaniline (A); 4-nitrophenol (B); 1-chloro-4-nitrobenzene (C); 1-bromo-4-nitrobenzene (D); 4-nitrotoluene (E) and 4-nitroanisole (F).

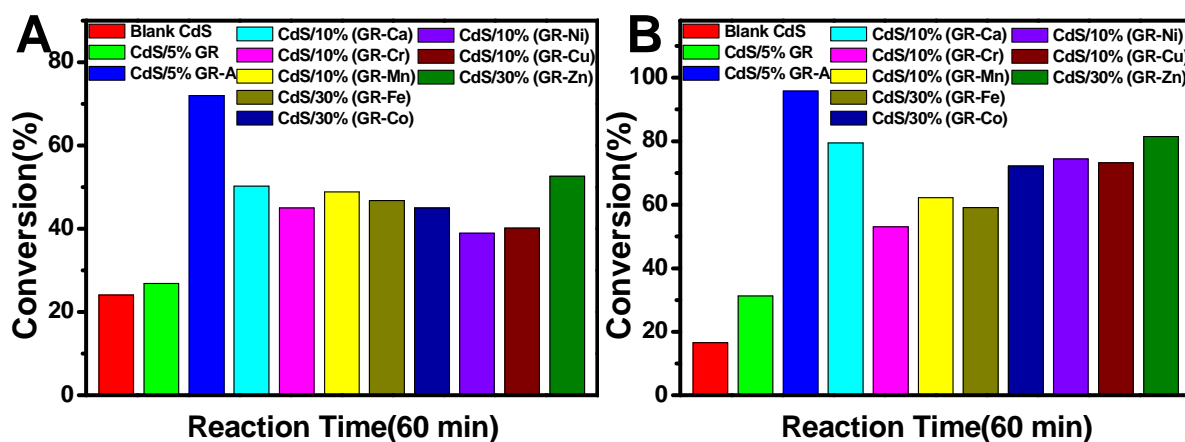
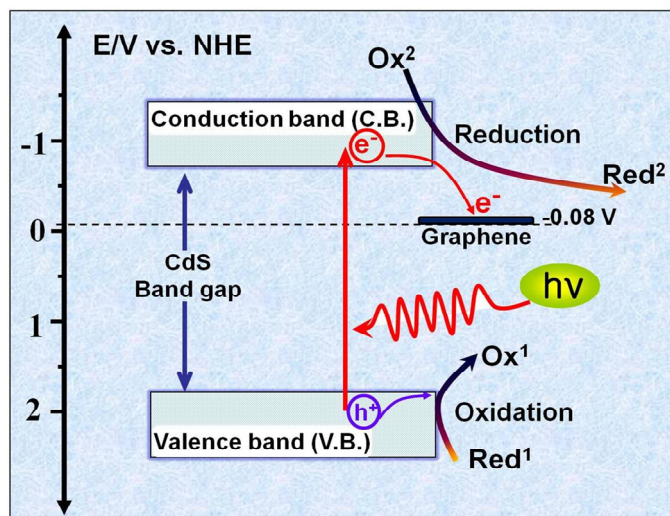


**Fig. S14.** Comparison of photocatalytic selective oxidation of benzyl alcohol to benzaldehyde (A) and reduction of 4-nitroaniline (4-NA) to p-phenylenediamine (B) over blank CdS, CdS/5% GR, CdS/5% GR-A and optimal CdS/(GR-M) (M = Ca<sup>2+</sup>, Cr<sup>3+</sup>, Mn<sup>2+</sup>, Fe<sup>2+</sup>, Co<sup>2+</sup>, Ni<sup>2+</sup>, Cu<sup>2+</sup>, and Zn<sup>2+</sup>) nanocomposites under visible light irradiation ( $\lambda > 420$  nm) for 60 min.

**Note:** The photocatalytic activity comparison in **Fig. S14** shows that toward the two probe reactions of selective oxidation of benzyl alcohol and reduction of 4-nitroaniline under identical reaction conditions, the CdS/GR-A also displays higher photoactivity than CdS-(GR-M) with the addition of metal ions as interfacial mediator proposed by our group recently.<sup>S1</sup> The comparison results further demonstrate that the ultrasonic treatment of GO with acid is a simple yet efficient approach to significantly improve the photoactivity of GR/semiconductor nanocomposites. In the as-reported literatures, GO is widely used as the precursor of GR to synthesize GR-based composite photocatalysts. The synthesis of GO are all based on the modified Hummers' method in different laboratories, but owing to the difference in the specific synthesis procedure, the size, shape and morphology of the prepared GO must be different from synthesis to synthesis. Our work has directly proven that such size, shape and morphology difference of GO would have a significant influence on the electronic conductivity of the reduced GR and the interaction between GR and semiconductor during the solution synthesis process, which thus affects the photocatalytic performance of the as-prepared GR-based composite photocatalysts. The result indicates that for designing more efficient GR/semiconductor composite photocatalysts, the physico-chemistry features (*e.g.*, the size, shape, morphology and colloidal stability) of the precursor GO are key and important factors that should be considered and optimized.



**Scheme S1.** Schematic description for photocatalytic redox processes over the CdS/graphene nanocomposites.

**Note:** Owing to the energy level match, graphene with high electronic conductivity and ballistic electron transport is able to accept, store and shuttle photogenerated electrons from semiconductor CdS under visible light irradiation.<sup>S1-S5</sup> Because GR-A displays much better electronic conductivity than GR, the separation and transfer of photogenerated charge carriers in the CdS/GR-A nanocomposites would be more efficient than that of the CdS/GR system as already discussed in our manuscript, which thus contributes to the remarkable improvement of the photocatalytic performance of CdS/GR-A toward artificial photoredox reactions as compared to that of CdS/GR.

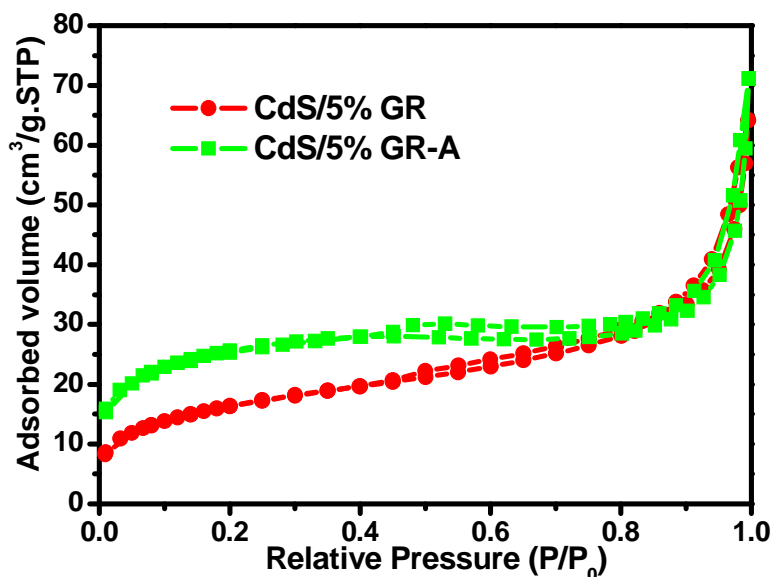


**Fig. S15.** N<sub>2</sub> adsorption-desorption isotherms of CdS/5%GR and CdS/5%GR-A.

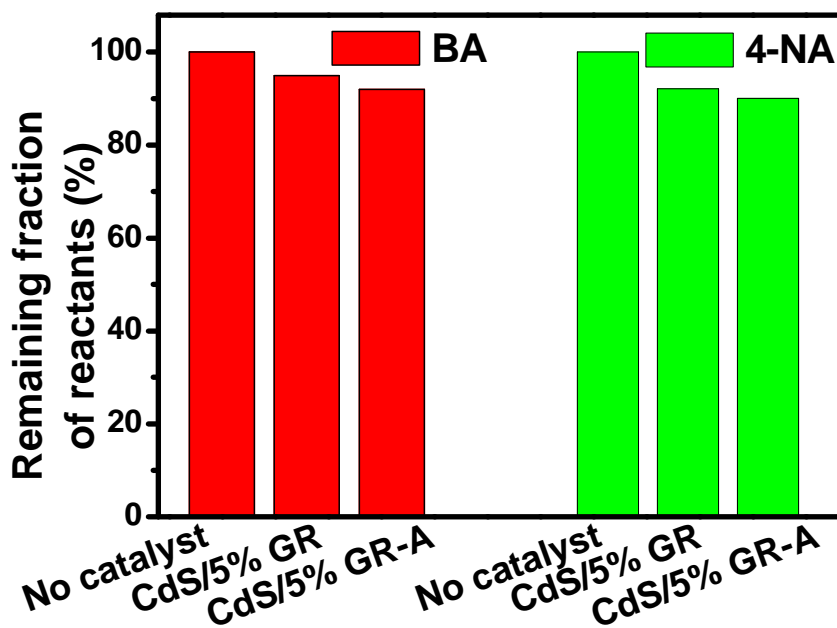


**Fig. S16.** Bar plot showing the remaining benzyl alcohol (BA) and 4-nitroaniline (4-NA) in reaction solution after being kept in dark for 2 h to achieve the adsorption-desorption equilibrium over CdS/5%GR and CdS/5%GR-A.

**Note:** Fig. S16 shows the result of adsorption experiments in the dark for benzyl alcohol (BA) and 4-nitroaniline (4-NA) over CdS/5%GR and CdS/5%GR-A nanocomposites. The result suggests that the CdS/5%GR-A displays slightly increased adsorptivity for the reactants than CdS/5%GR, which is consistent with its higher surface area. Since the semiconductor-based heterogeneous photocatalysis is a surface-based process,<sup>S6</sup> the increased adsorptivity of reactants of CdS/5%GR-A is believed to be also beneficial for improving the photocatalytic performance under the visible light irradiation.

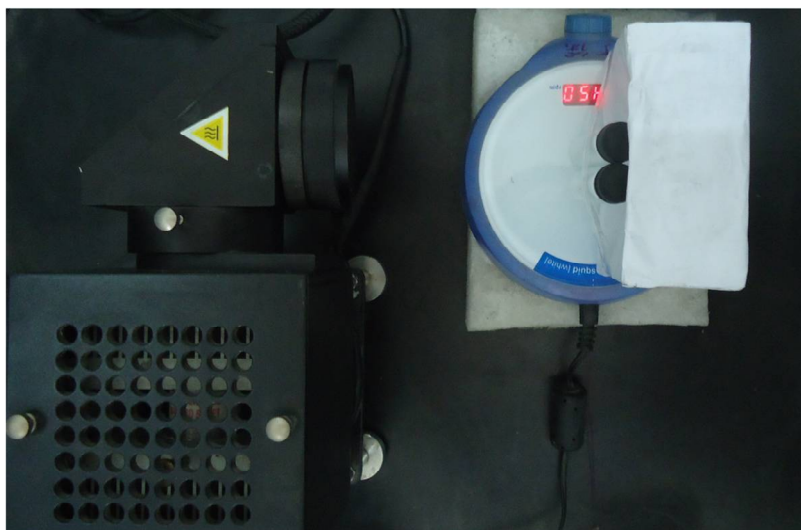


**Fig. S17.** Photograph of the experimental setup for photocatalytic aerobic oxidation of alcohols.

**Note:** The photocatalytic selective oxidation of benzylic alcohols was performed in 10 mL Pyrex glass bottle, as shown in **Fig. S17**. This simple experimental setup for photocatalytic aerobic oxidation of alcohols has also been utilized in the previous work reported by Zhao's group.<sup>S7,S8</sup>



**Fig. S18.** Photograph of the experimental setup for photocatalytic anaerobic reduction of nitroaromatic compounds.

## References

- (S1) N. Zhang, M.-Q. Yang, Z.-R. Tang and Y.-J. Xu, *ACS Nano*, 2014, **8**, 623-633.
- (S2) N. Zhang, Y. Zhang, X. Pan, M.-Q. Yang and Y.-J. Xu, *J. Phys. Chem. C*, 2012, **116**, 18023-18031.
- (S3) N. Zhang, Y. Zhang, M.-Q. Yang, Z.-R. Tang and Y.-J. Xu, *J. Catal.*, 2013, **299**, 210-221.
- (S4) F.-X. Xiao, J. Miao and B. Liu, *J. Am. Chem. Soc.*, 2014, **136**, 1559-1569.
- (S5) Q. Li, B. Guo, J. Yu, J. Ran, B. Zhang, H.-J. Yan and J. R. Gong, *J. Am. Chem. Soc.*, 2011, **133**, 10878-10884.
- (S6) M.-Q. Yang, N. Zhang, M. Pagliaro and Y.-J. Xu, *Chem. Soc. Rev.*, 2014, **43**, 8240-8254.
- (S7) M. Zhang, C. Chen, W. Ma and J. Zhao, *Angew. Chem. Int. Ed.*, 2008, **47**, 9730-9733.
- (S8) M. Zhang, Q. Wang, C. Chen, L. Zang, W. Ma and J. Zhao, *Angew. Chem. Int. Ed.*, 2009, **48**, 6081-6084.